

# SPECTRAL MODELING OF THE CHARGE-EXCHANGE X-RAY EMISSION FROM M82

SHUINAI ZHANG

Purple Mountain Observatory, CAS, Nanjing, 210008, China and  
 Key Laboratory of Dark Matter and Space Astronomy, CAS, Nanjing 210008, China

Q. DANIEL WANG

Astronomy Department, University of Massachusetts, Amherst, MA01003, USA

LI JI

Purple Mountain Observatory, CAS, Nanjing, 210008, China and  
 Key Laboratory of Dark Matter and Space Astronomy, CAS, Nanjing 210008, China

RANDALL K. SMITH AND ADAM R. FOSTER

Harvard-Smithsonian Center for Astrophysics, Cambridge, MA 02138, USA

AND

XIN ZHOU

Purple Mountain Observatory, CAS, Nanjing, 210008, China and  
 Key Laboratory of Radio Astronomy, CAS, Nanjing 210008, China

*Submitted May 18, 2014. Accepted for publication in Astrophysical Journal, August 12, 2014*

## ABSTRACT

It has been proposed that the charge exchange (CX) process at the interface between hot and cool interstellar gases could contribute significantly to the observed soft X-ray emission in star forming galaxies. We analyze the *XMM-Newton*/RGS spectrum of M82, using a newly developed CX model combined with a single-temperature thermal plasma to characterize the volume-filling hot gas. The CX process is largely responsible for not only the strongly enhanced forbidden lines of the K $\alpha$  triplets of various He-like ions, but also good fractions of the Ly $\alpha$  transitions of C VI ( $\sim 87\%$ ), O VIII and N VII ( $\gtrsim 50\%$ ) as well. In total about a quarter of the X-ray flux in the RGS 6-30 Å band originates in the CX. We infer an ion incident rate of  $3 \times 10^{51} \text{ s}^{-1}$  undergoing CX at the hot and cool gas interface, and an effective area of the interface as  $\sim 2 \times 10^{45} \text{ cm}^2$  that is one order of magnitude larger than the cross section of the global biconic outflow. With the CX contribution accounted for, the best fit temperature of the hot gas is 0.6 keV, and the metal abundances are approximately solar. We further show that the same CX/thermal plasma model also gives an excellent description of the EPIC-pn spectrum of the outflow Cap, projected at 11.6 kpc away from the galactic disk of M82. This analysis demonstrates that the CX is potentially an important contributor to the X-ray emission from starburst galaxies and also an invaluable tool to probe the interface astrophysics.

*Subject headings:* galaxies: individual (M82) — galaxies: starburst — X-rays : galaxies

## 1. INTRODUCTION

Galaxy-scale outflows (sometimes called superwinds) driven by supernovae (SNe) are ubiquitous in starburst galaxies (e.g., Heckman et al. 1990; Heckman 2005). Such outflows represent a primary mechanism of stellar feedback, which injects energetic and chemically enriched materials into the circum-galactic medium (CGM) or even the intergalactic medium (IGM) (Veilleux et al. 2005). The outflows consist of multiphases, including X-ray-emitting thermal plasma (e.g., Bregman et al. 1995; Griffiths et al. 2000), warm ionized gas (Shopbell & Bland-Hawthorn 1998), neutral atomic/molecular gas, and dust (Lehnert et al. 1999; Taylor et al. 2001), as shown in M82 — the target galaxy of the present study.

As a prototype starburst-driven outflow, M82 has received some of the most extensive studies of individual galaxies. The salient parameters of the galaxy are listed

in Table 1. The outflow from the nuclear region of the galaxy extends at least 3 kpc away on both sides from the galactic disk along its minor axis. It is widely assumed that the outflow is driven by volume-filling hot plasma, while cold and warm gases are entrained within the flow (e.g., Chevalier & Clegg 1985). Little is actually known about the origin of the emission lines and hence about the properties of the hot plasma and its interplay with the cool components. The soft X-ray emission ( $\sim 0.5$ -1 keV), in particular, may arise from either the volume-filling hot outflow (Fabbiano 1988; Bregman et al. 1995) or mostly from the cool-hot gas interface with a very low volume-filling factor (Strickland & Stevens 2000a; Strickland et al. 2002). Without separating these very different contributions, one cannot determine the energetics, as well as the thermal and chemical properties of the hot plasma, hence the potential role of the outflow in regulating the evolution of the galaxy and its environment.

High resolution X-ray spectroscopy offers an oppor-

tunity to greatly advance our understanding of galactic outflows. Here we use the *XMM-Newton* Reflection Grating Spectrometer (RGS) observations of M82 to demonstrate this potential. Although the X-ray emission from the galaxy is extended, the large wavelength dispersion of the RGS still allows us to detect or resolve key individual X-ray emission lines or complexes, such as  $K\alpha$  triplets of He-line ions, with confusion far less than that in an X-ray CCD spectrum (e.g., extracted from *XMM-Newton*/European Photon Imaging Camera (EPIC) data). Indeed, existing studies with the RGS data have already demonstrated the diagnostic power of the line spectroscopy. In the analysis of a 50 ks RGS observation of M82, Ranalli et al. (2008) found that the O VIII  $Ly\alpha$  line and the O VII  $K\alpha$  triplet cannot be appropriately accounted for even with a multi-temperature thermal plasma model and argued that the O VII triplet may indicate a significant contribution from charge exchange (CX) (Beiersdorfer et al. 2003). This process occurs when an ion captures an electron from a neutral atom or molecule. The captured electron tends to be in an excited state; the subsequent downward cascades can produce emission lines with relative intensities distinctly different from a collisionally excited plasma (Foster et al. 2012). Liu et al. (2012) quantified the CX contributions by analyzing individual line components of the  $K\alpha$  triplets of Helium-like O, Ne and Mg ions. Because of the electron capture, CX contributes to the line emission from lower ionization states than in equilibrium thermal plasma; in the case of multiple CX reactions, the emission appears at increasingly lower ionization states. Therefore, the spectral analysis of the emission arising even partly from the CX could lead to very misleading results on the temperature and chemical properties of the plasma, if only its thermal (collisionally-excited) emission is considered. CX may also contribute significantly to the enhanced X-ray emission from the so-called outflow Cap, projected at 11.6 kpc away from the galactic disk of M82 (Lallement 2004). This X-ray enhancement coincides with an H $\alpha$ -emitting filament (Devine & Bally 1999), which is also seen in ultraviolet emission due to the reflection by dust (Hoopes et al. 2005). Although the X-ray CCD spectra obtained from *Suzaku* and *XMM-Newton* observations are well characterized by two-temperature components of optically-thin thermal plasma, it has been suggested that some of the observed emission lines could be due to the CX (Tsuru et al. 2007).

In this paper, we take a step further to model the entire RGS spectrum of M82, accounting for both thermal and CX contributions simultaneously. We assume a volume-filling, single-temperature, optically-thin plasma in collisional ionization equilibrium, which is responsible for the thermal emission, and an interface of the plasma with cool gas, where the CX occurs. This simple model is particularly motivated by the development of an integrated CX spectral code (Smith et al. 2012). We check how well the RGS spectrum can be fitted with the model and what constraints can be obtained on the effectiveness of the CX process or the effective interface area, as well as the properties of the thermal plasma. We further apply the model to the analysis of an *XMM-Newton*/EPIC-pn spectrum of the Cap region to check the consistency of the model and to infer the dynamics of the outflow.

TABLE 1  
PARAMETERS OF M82

Parameter	Value	Ref. <sup>a</sup>
RA(J2000.0)	09:55:52.7	1
Dec(J2000.0)	+69:40:46	1
Distance	3.52 Mpc	2
Scale	1.02 kpc/arcmin	2
Redshift	0.000677	1
Disk Inclination	81.5°	3
Star Formation rate	$\sim 5 M_{\odot} \text{ yr}^{-1}$	4

<sup>a</sup> References: 1, NASA/IPAC Extragalactic Database (NED, <http://ned.ipac.caltech.edu>); 2, Jacobs et al. (2009); 3, Lynds & Sandage (1963); 4, Strickland & Heckman (2009).

The organization of the paper is as follows: We describe the RGS data and model in sections 2 and 3, We present the fitting results in section 4 and explore their implications in section 5, characterizing the key parameters of the hot gas outflow and its interplay with the cool gas.

## 2. XMM-NEWTON DATA

The present study uses the longest (104 ks) *XMM-Newton* observation (ID: 0206080101) of M82. After removing time intervals of high background with a counting rate above 0.2 counts  $\text{s}^{-1}$  in the energy band above 10 keV, the remaining effective exposure is 50 ks. We extract RGS spectra from the exposure, using the standard ‘rgsproc’ script of SAS (version 12.0.0) and the 98% cross-dispersion (roughly 2 arcmin) width of the point spread function. The zero point position of the dispersion is set at the center of the galaxy disk of M82 (Table 1). The script also produces a simulated background spectrum based on blank-sky observations. We combine the RGS1 and RGS2 spectra into one spectrum by the ‘rgscombine’ script, and regroup it with at least 20 photons per bin to allow for  $\chi^2$  fitting, which uses the Interactive Spectral Interpretation System (ISIS version 1.6.2, Houck 2002) that includes all Xspec models.

The RGS spectrum covers the wavelength range of 6-30 Å (or 0.41-2.07 keV). Since the RGSs are slitless spectrometers, the extracted spectra are a convolution of the line spread function with the (projected) intrinsic spatial distribution of the X-ray emission. The dispersion of the RGSs is 0.138 Å per arcmin for a point-like source (den Herder et al. 2001). For the RGS observation with a position angle of 319.3°, the dispersion direction is roughly along the long axis of the outflow, or the minor axis of M82, toward the northwest (Fig. 1a). As a result, the profile of an intrinsically narrow emission line (e.g., Fig. 1b) is determined chiefly by the extension of the outflow. The blue and red sides of the line correspond to the northern and southern components of the outflow, respectively. This line broadening is considered in the RGS spectral analysis (see § 3.2).

We further extract an EPIC-pn spectrum of the Cap from the same *XMM-Newton* observation. The data are processed with the standard procedures of SAS. Time intervals with counting rates above 0.7 counts  $\text{s}^{-1}$  in the energy band above 10 keV are removed to minimize the contamination of high non-X-ray background, resulting in a total effective exposures of 51 ks. For the spec-

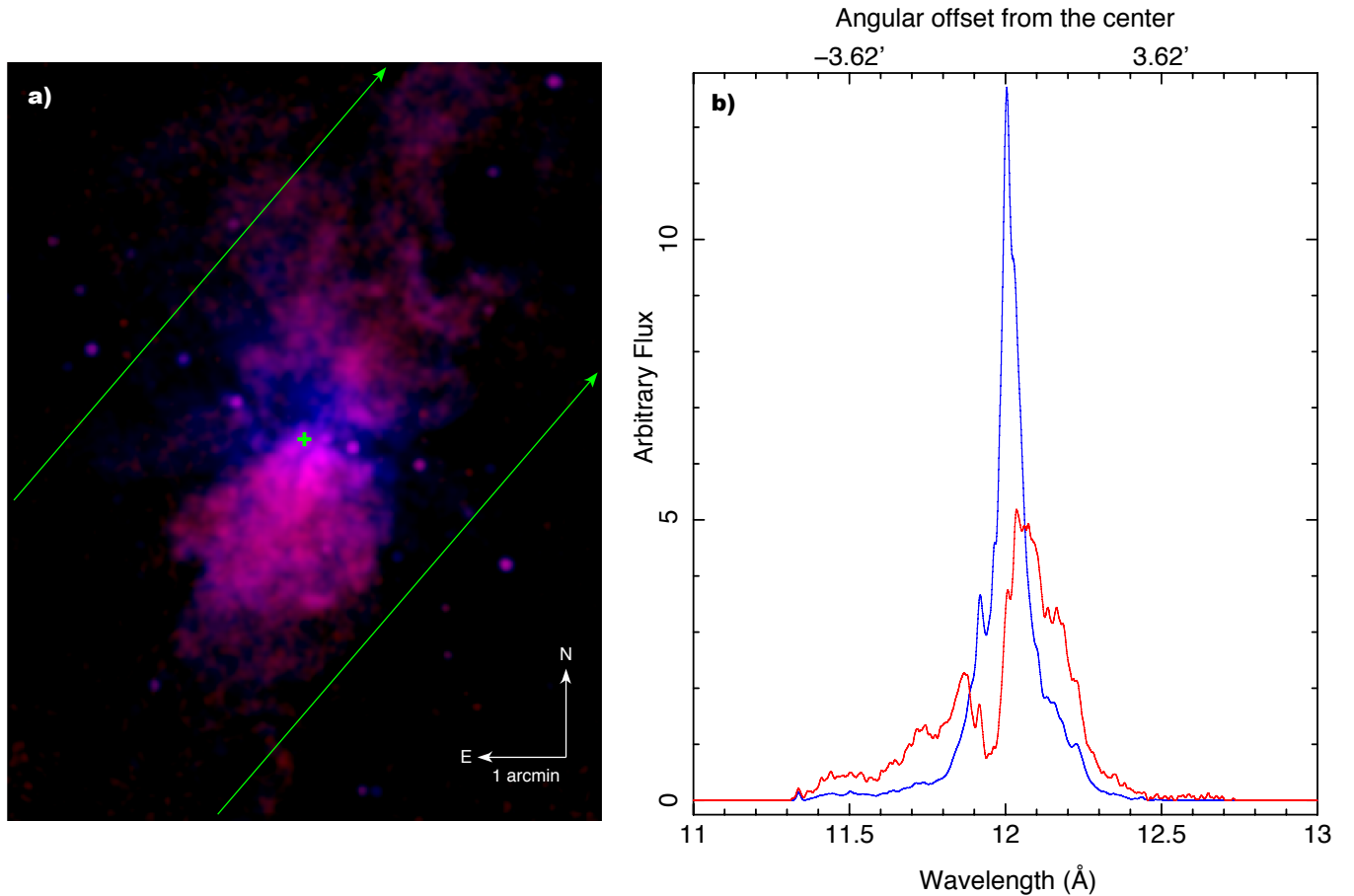


FIG. 1.— (a) *Chandra* images of the two bands, where the blue color marks the hard band (6-18 Å) and the red color marks the soft band (20-30 Å). The cross point is the center of M82. The RGS spectral extraction is between the two green lines, while the arrows mark the direction of the RGS dispersion. (b) Broadening profiles for a narrow Gaussian line (centered at 12 Å for an illustration), convolved with the two images. The blue line shows the profile from the hard band image, and the red line from the soft band image.

tral extraction, we adopt source and background regions that are nearly identical to those used by Tsuru et al. (2007) for the same observation. The extracted spectrum is grouped so that each bin contains a minimum signal-to-noise ratio of 3 in the 0.3-2 keV band.

### 3. SPECTRAL MODELING

Table 2 summarizes the model composition used to characterize the spectra of the outflow and the Cap. For the outflow, the model consists of: (1) a volume-filling, single-temperature plasma, which not only contributes to the optically-thin thermal emission, but also sets the ionization states of ions before the CX occurs; (2) the CX emission from the interface; (3) the continuum emission from point sources in the field, such as M82 X-1 (Matsumoto et al. 2001). The components (1) and (3) are represented by an APEC (Astrophysical Plasma Emission Code; Foster et al. 2012) and a power law. We fix the power law photon index as  $\Gamma = 1.6$  from fitting the EPIC-pn spectrum of the central region of M82 (Ranalli et al. 2008), which is sensitive primarily to the energy range  $\gtrsim 2$  keV (higher than that covered by the RGS data), where the confusion with the diffuse X-ray emission from the hot gas is minimal. The normalization of the power law is allowed to vary, depending on the specific field covered by the RGS spectrum. Key elemental abundances are also allowed to vary, rela-

tive to the solar abundances (Anders & Grevesse 1989). In addition to a common, fixed Galactic absorption of  $N_{\text{H}} = 4.0 \times 10^{20} \text{ cm}^{-2}$  (Dickey & Lockman 1990), intrinsic absorption is allowed for the (1)+(2) and (3) components separately. This absorption is characterized by the model TBABS (Wilms et al. 2000), assuming the same solar abundances. For the Cap, no intrinsic absorption is assumed and the abundances of the plasma are the same as those that best fits the outflow spectrum.

In the following, we concentrate on describing the newly developed CX spectral model and the approach used to account for the line broadening due to the extended nature of the diffuse plasma.

#### 3.1. CX modeling

Smith et al. (2012) have presented an approximate model for the CX process and the subsequent electron cascading down in energy levels, resulting in a predicted emission spectral model. While the details can be found in the work by Smith et al. (2014) (or online<sup>1</sup>), we here present a brief outline of the model.

The model assumes the most probable CX process that only a single electron is captured by an ion. The process

<sup>1</sup> [www.atomdb.org/CX/](http://www.atomdb.org/CX/)

TABLE 2  
SUMMARY OF SPECTRAL RESULTS

Instruments	Outflow (RGS)	Cap (EPIC-pn)
XSPEC Model <sup>a</sup>	A(G)[A(c) PL+A(o)(APEC*+CX*)]	A(G)(APEC+CX)
$N_{\text{H}}^{\text{G}}$ (cm <sup>-2</sup> )	$4 \times 10^{20}$ (fixed)	-
$N_{\text{H}}^{\text{c}}$ (cm <sup>-2</sup> )	$3.5(\pm 0.3) \times 10^{21}$	-
$N_{\text{H}}^{\text{o}}$ (cm <sup>-2</sup> )	$1.3(\pm 0.2) \times 10^{21}$	-
PL photon index	1.6 (fixed)	-
Norm (APEC)	$6.2(\pm 1.2) \times 10^{-3}$	$5.2(\pm 0.8) \times 10^{-5}$
Norm (CX)	$2.1(\pm 0.3) \times 10^{-5}$	$4.1(\pm 0.7) \times 10^{-7}$
$k_{\text{B}}T$ (keV)	$0.60 \pm 0.01$	$0.58 \pm 0.09$
C	$0.41 \pm 0.37$	0.41 (fixed)
N	$0.85 \pm 0.17$	0.85 (fixed)
O	$0.56 \pm 0.05$	0.56 (fixed)
Ne	$1.21 \pm 0.13$	1.21 (fixed)
Mg	$1.18 \pm 0.13$	1.18 (fixed)
Si	$2.35 \pm 0.32$	2.35 (fixed)
Fe	$0.31 \pm 0.03$	0.31 (fixed)
Separate fitting abundance ratios <sup>b</sup>		
C/Fe	$1.32 \pm 1.31$	-
N/Fe	$2.74^{+0.83}_{-0.59}$	-
O/Fe	$1.80 \pm 0.20$	-
Ne/Fe	$3.90 \pm 0.32$	-
Mg/Fe	$3.81 \pm 0.53$	-
Si/Fe	$7.58^{+1.58}_{-0.84}$	-
$\chi^2/\text{d.o.f.}$	1.61 (1862.0/1158)	1.20 (69.8/58)

\* The models are convolved with line profiles generated from *Chandra* images.

<sup>a</sup> A(G), A(c), or A(o) stand for the absorption (TBABS) by the Galactic foreground (G), gas intrinsic to the central region (c), or to the outflow region (o) of M82, with the corresponding column density of  $N_{\text{H}}^{\text{G}}$ ,  $N_{\text{H}}^{\text{c}}$ , or  $N_{\text{H}}^{\text{o}}$ .

<sup>b</sup> From a separate fitting with the Fe abundance fixed to the above best fit value.

<sup>note</sup> Chemical abundances are relative to solar values.

can be represented by

$$\text{A}^{q+} + \text{N} \rightarrow (\text{A}^*)^{(q-1)+} + \text{N}^+,$$

where a highly ionized ion  $\text{A}^{q+}$  (such as O VIII and Ne X) picks up an electron from a neutral species N (H, H<sub>2</sub>, and/or He), producing an excited ion  $(\text{A}^*)^{(q-1)+}$ , which emits X-ray photons as it decays to the ground state.

The emission spectrum depends on the relative  $n$  and  $l$  distribution of the captured electrons, which affects the transitions during the subsequent electron cascade to the ground state. The principal  $n$  shell for the electron capture is determined from Equation 2.6 of Janev & Winter (1985). The orbital angular momentum  $l$  is more complex: several distributions are available, each roughly corresponding to different center-of-mass velocities of the system. At lower collision energies, the separable  $l$  distribution is suitable (Equation 3.59 of Janev & Winter 1985). Once captured, the electron cascades down to the ground state, purely by spontaneous or two photon emission. The model calculation includes a complete set of ions and radiative transitions based on the AtomDB database (Foster et al. 2012). Therefore, the calculated emission spectrum can then be directly compared to an observed one.

We consider two extreme electron capture modes regarding to whether or not an ion can have at most one CX. In one case, we assume that only one electron is captured. This is for CX in a sea of ions meeting oc-

casional individual neutral atoms which have penetrated into the hot “wind”, a circumstance suitable for the solar wind (Smith et al. 2014). In another case, the “standard” one, multiple CX captures occur rapidly until the ion becomes neutral, an assumption justified by the large cross section for CX - typically several orders of magnitude higher than the electron-ion collisional excitation cross sections. The difference between the two cases is mainly reflected by the H- and He-like ion ratios (due to one or two CX captures) for C, N, O, and Ne. The prominent lines from Li-like ions are usually with energies lower than 0.3 keV, therefore are not in an RGS spectrum.

The cold gas in the outflow of M82 is either clouds entrained by the hot gas or the inflows due to the interaction with M81 (Melioli et al. 2013). In the infrared band image of M82, the thickness of the filaments and shells of the cold gas are normally on the scale of several 10 pc (Engelbracht et al. 2006), much greater than the mean free path of the CX that occurs at the immediate vicinity of the interface due to its large cross-section (typically a few  $\times 10^{-15}$  cm<sup>2</sup>). Thus, the situation in M82 is probably more suitable for the multiple CX case, in which the normalization parameter is physically meaningful as

$$\eta = 10^{-5} f_{\text{H}} / [4\pi D_{\text{A}}^2 (1+z)^2],$$

where  $D_{\text{A}}$  and  $z$  are the angular diameter distance and the cosmic redshift of the target, while  $f_{\text{H}} = \int n_{\text{H}} v dS$  is

the equivalent (metal abundance-dependent) hot proton incident rate (in units of protons  $\text{s}^{-1}$ ) through the interface. When the normalization is determined in a fit to the observed spectrum,  $f_{\text{H}}$  can then be measured. Furthermore, if the proton density  $n_{\text{H}}$  of the hot plasma and the velocity  $v$  (of ions relative to neutral atoms) can be estimated, one can then infer the effective area of the interface in the spectral extraction region.

### 3.2. RGS line profile modeling

We use the Xspec convolution model RGSXSRC to account for the spectral broadening caused by the spatial distribution of the X-ray emission. We approximate the energy-dependent distribution using two high-resolution diffuse X-ray intensity images, constructed from mosaicing 30 *Chandra* ACIS observations of M82 in the 6-18 Å (hard) and 20-30 Å (soft) bands and smoothed with a Gaussian filter of FWHM=5'. Figure 1a shows that the X-ray intensity is quite concentrated (within the inner 1.5 arcmin radius) in the hard band and is considerably more extended in the soft band. The lack of the emission near the galactic disk in this soft band is due to the strong photoelectric absorption by the interstellar medium (ISM) in M82. The convolution of the RGSXSRC model uses the same dispersion center coordinates and position angle as for the RGS spectrum, as well as an aperture radius of 4 arcmin, as suggested by Ranalli et al. (2008), to cover the bulk of the emission from the outflow.

Figure 1b demonstrates the spectral line broadenings as predicted from the above described convolution of a Gaussian emission line (12 Å) with a turbulent velocity of 100  $\text{km s}^{-1}$ . The hard band image, where the thermal emission dominates, is used for the convolution with the APEC model. The CX contribution (Liu et al. 2012) becomes increasingly important and even dominates at longer wavelengths. Thus the CX model is convolved with the soft band image. The dip near the center of this line profile reflects the absorption by the ISM.

## 4. RESULTS

Figure 2 presents the RGS spectrum of M82 and the best fit model. A close-up of the O VII and O VIII line complex is given in Figure 3, showing the CX contributions to individual lines. In particular, the O VII forbidden line is well fitted by the CX contribution. A small residual at 21.4 Å on the shorter wavelength side of the O VII(r) is probably due to uncertainties in the derived line profiles.

Table 2 includes our best fit model parameters and their uncertainties at the 90% statistical confidence level. The overall CX flux contribution is about one third of the thermal emission in the 6-30 Å range and dominates at wavelengths  $\gtrsim 20$  Å. In Table 3, we further compare the fluxes of the continuum, thermal, and CX components of the model. Systematic errors likely dominate in our simple model characterization of the X-ray spectrum. To quantify such errors, we measured fluxes for major individual lines or complexes in the observed spectrum and compare the results with those in the best fit model (Table 4). The CX to total line flux ratio ranges from 87% for the O VII triplet to less than 3% for Fe XVII (16.9 Å). The 'goodness' parameter represents the percentage

TABLE 3  
FLUXES OF INDIVIDUAL COMPONENTS

Flux <sup>a</sup>	Outflow	Cap
PL (X-ray)	$7.3 \times 10^{-12}$	-
APEC (X-ray)	$9.6 \times 10^{-12}$	$8.2 \times 10^{-14}$
CX (X-ray)	$3.7 \times 10^{-12}$	$6.9 \times 10^{-14}$
CX (H $\alpha$ )	$1.3 \times 10^{-12}$	$2.5 \times 10^{-14}$
Total (H $\alpha$ )	$4.6 \times 10^{-11}$	$1.5 \times 10^{-13}$
Ion Incident Rate	$3.2 \times 10^{51}$	$6.2 \times 10^{49}$

<sup>a</sup> The ion incident rate is in units of  $\text{s}^{-1}$ , whereas the photon energy fluxes are all in units of  $\text{erg cm}^{-2}\text{s}^{-1}$ . The X-ray fluxes are measured in the range of 6-30 Å. The total H $\alpha$  fluxes from Lehnert et al. (1999) are included for comparison.

of the line flux (in the observed spectrum) that is accounted for by the thermal+CX line component of the model. The deviation from the ideal value (100%) are all within 25%, except for Mg XII line (40%). Considering the uncertainties in the theoretical transition rates of the lines ( $\sim 30\%$ ; Guennou et al. 2013) and the simplicity of our model, we conclude that the fitting is remarkably good ( $\chi^2/n.d.f. = 1.61$ , including only statistical errors).

The metal abundances, except for Si and Fe, all seem to be consistent with being solar within a factor of 2, counting the statistical uncertainties (Table 2). The abundances of C, N and O are about 0.6 solar; Ne and Mg about 1.2, Si 2.4, and Fe is 0.3. These measurements do not seem to be sensitive to various potential systematic uncertainties. For example, fixing the power law index  $\Gamma$  from 1.4 to 1.8 results in a change of individual elemental abundance to be less than 0.1. Nevertheless, in the soft X-ray range considered here, it is difficult to accurately determine the absolute abundances relative to H, because H only contributes to the continuum. Instead, the data are more sensitive to the relative abundances among metal elements. We thus also measure the abundances relative to Fe by setting their ratios as free parameters. The resulting abundance ratios, included in Table 2, are all supersolar, but within a factor of 4, except for the Si to Fe ratio, which is about 8 times higher.

We find that the above APEC+CX model, which best fits the RGS spectrum of the outflow region, also characterizes the pn spectrum of the Cap well. Because it is far away from the disk of M82, we exclude the power law and the intrinsic absorption. The metal abundances are fixed to the best fit values of the RGS spectrum, which is reasonable because the X-ray emission at the Cap is presumably induced by the outflow plasma from the vicinity of the galactic disk. We first only allow the normalizations of the APEC and CX components to vary, which gives  $\chi^2/d.o.f. = 1.20(70.6/59)$ . We then also let the temperature of the plasma vary, which yields slightly changes (well within the statistical uncertainties). The results of this latter fit are included in Table 2, and the plot is presented in Figure 4. The flux contributions from the APEC and CX components to the spectrum of the Cap are comparable to each other (Table 3).

## 5. DISCUSSION

The above results demonstrate an apparent success of the APEC+CX modeling of the line emission from the

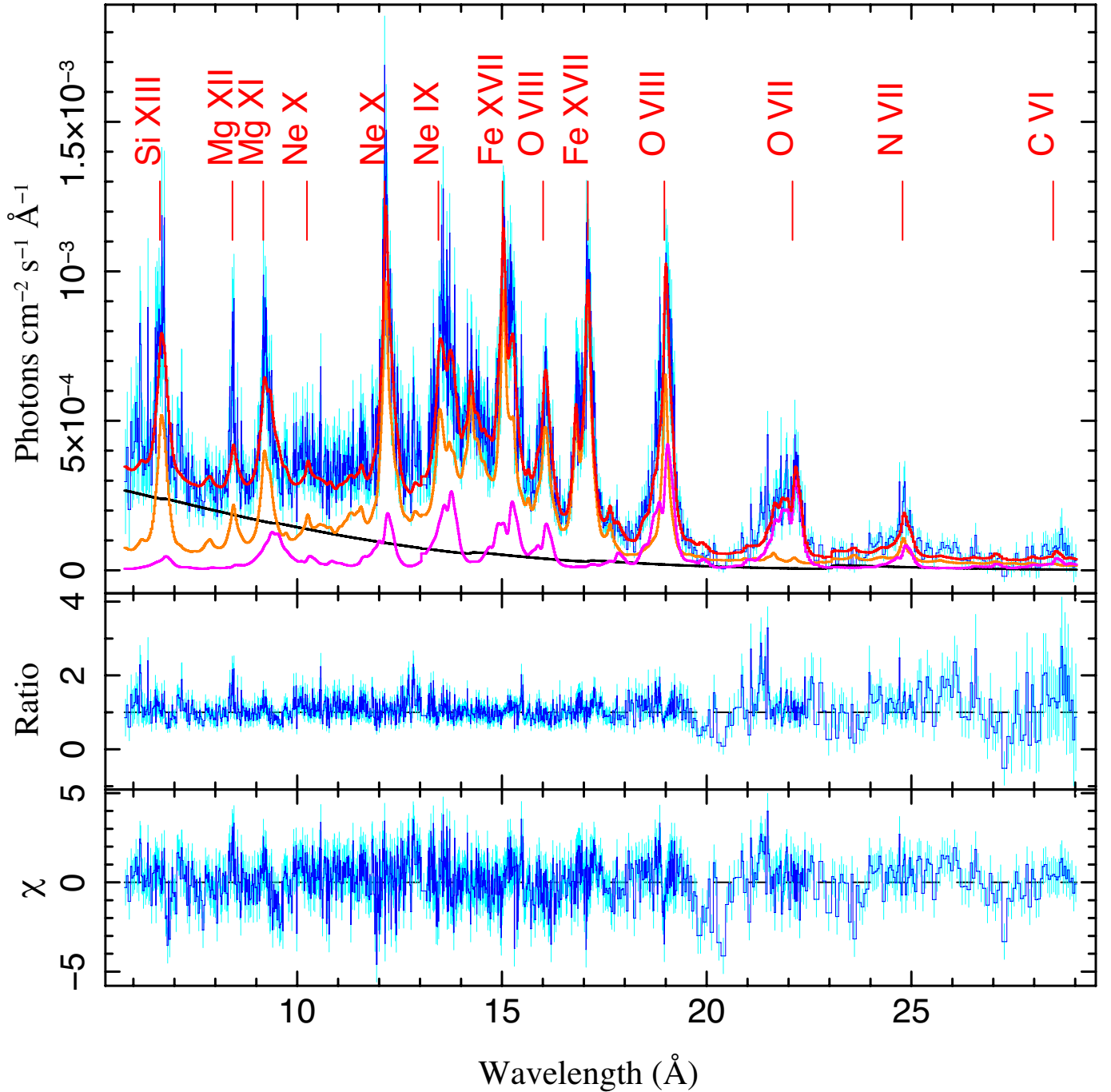


FIG. 2.— RGS spectrum of M82 and the best fit model (red curve). The two lower panels show the data to model ratio and the data-model residuals (divided by the counting error in each bin). The three emission components are power law (black), thermal plasma (orange), and CX (purple).

outflow and the consistency in explaining the overall X-ray spectrum of the Cap with the same model. In this section, we explore the implications of the results for understanding the hot plasma and its interface with the cool gas.

##### 5.1. Properties of the hot plasma

The accounting for the CX contribution leads to an improved characterization of the thermal and chemical properties of the volume-filling hot plasma. So far the most sophisticated modeling of the RGS spectra without the CX uses thermal plasma with multiple or distributed

temperature components. Close to the peak temperature of such modeling (e.g., 0.7 keV from Read & Stevens 2002 or from Origlia et al. 2004; 0.5 keV from Ranalli et al. 2008) is our best fit effective temperature of 0.6 keV (with the CX accounted for). The CX process contributes more at longer wavelength, playing a role similar to the low temperature components in the plasma-alone modeling.

Given the temperature, we can estimate the mass loading factor  $\beta$  that characterizes the amount of mass loaded from ISM to the hot gas in units of the net mass injection rate of SNe and stellar winds (SWs) from massive stars.

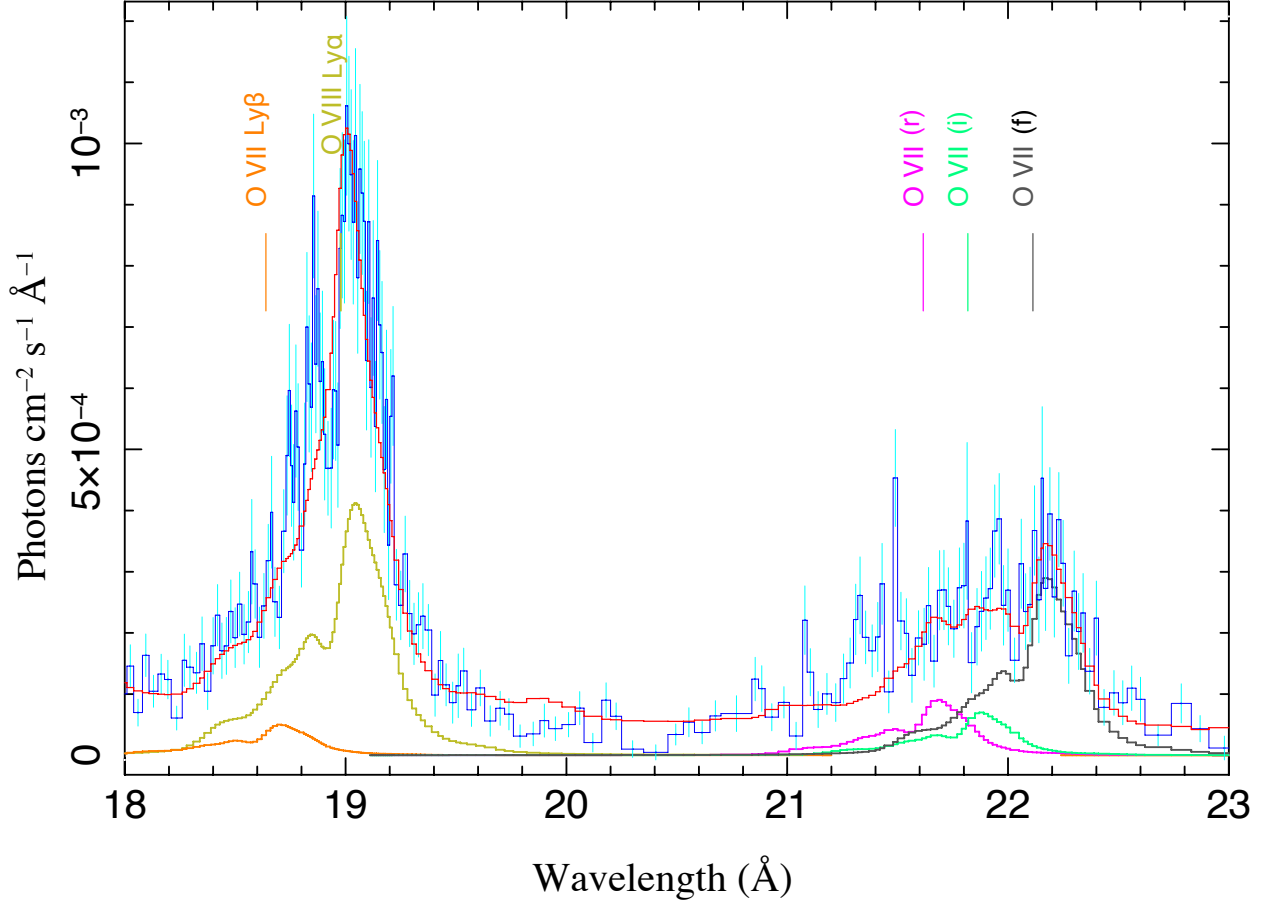


FIG. 3.— Close-up of the RGS spectrum in the wavelength range covering O VII and O VIII lines. The red curve is the total model prediction as in Fig. 2. The CX contributions to various transitions are now plotted separately: the purple, green, and grey curves represent the resonance, inter-combination, and forbidden components of the O VII  $K\alpha$  triplet, respectively, whereas the orange and golden curves mark the contributions to the O VII  $Ly\beta$  and O VIII  $Ly\alpha$  lines.

The temperature of the mass-loaded hot gas is

$$T = 0.4 \frac{\mu m_H \epsilon \dot{E}_{SN+SW}}{k \beta \dot{M}_{SN+SW}},$$

where  $\mu m_H \approx 1.02 \times 10^{-24} \text{ g cm}^{-3}$  is the mean mass per particle (taking the solar elemental abundances), and  $\epsilon$  is the mean thermalization efficiency of the kinetic energy released by SNe and SWs, assuming that the radiative cooling is not significant in the region (Mathews & Baker 1971). Strickland & Heckman (2009) calculated that the total SN plus SW energy and mass injection rates are  $3.1 \times 10^{42} \text{ erg s}^{-1}$  and  $1.4 M_\odot \text{ yr}^{-1}$  respectively, assuming a continuous star formation with a rate of  $4.7 M_\odot$  per year. They also constrained the mean thermalization efficiency to be  $30\% \leq \epsilon \leq 100\%$  based on hydrodynamics simulations. We adopt a middle value  $\epsilon = 70\%$ . As a result, a mass loading factor of  $\beta \sim 10$  is required to account for our inferred plasma temperature of 0.6 keV. In comparison, the mass loading factor within the  $\sim 500 \text{ pc}$  starburst region is estimated as  $1.0 \leq \beta \leq 2.8$  (Strickland & Heckman 2009). Based on hydrodynamics

simulations of the outflow, Suchkov et al. (1996) gives another estimate of the central mass loading factor as  $\sim 3 - 6$ . If all these estimates are reasonable, then the comparison suggests that the mass-loading process occurs primarily in the path of the outflow within  $\pm 3 \text{ kpc}$ . Alternatively, the low temperature plasma, as modeled here, may represent only part of the outflow, which has undergone substantial mass-loading (e.g., accompanied by CX). The rest of the outflow may have had little mass-loading and may thus have too high (low) a temperature (density) to contribute significantly to the spectrum. In any case, our one-temperature APEC modeling is meant to provide only a simple characterization of the thermal plasma responsible for the observed soft X-ray emission via both collisional excitation and CX.

Figure 5 compares our measurements of the abundance pattern with those from RGS (Ranalli et al. 2008) and *Suzaku* XIS (Konami et al. 2011) studies of M82. Take the work by Ranalli et al. (2008) as an example. Their estimate of the N abundance or the upper limit of O is obtained from fitting the N VII (25 Å) or O VIII (19 Å) line only, while the C abundance is not measured be-

TABLE 4  
FLUXES OF KEY LINE FEATURES (IN UNITS OF  $10^{-13} \text{ erg s}^{-1} \text{ cm}^{-2}$ )

Line features <sup>a</sup> ( $\lambda$ )	Range ( $\text{\AA}$ )	Data	Conti <sup>b</sup>	Thermal <sup>c</sup>	CX	Goodness <sup>d</sup>
Si XIII(6.65 $\text{\AA}$ )	6.4-7.0	$9.56 \pm 0.38$	4.52	5.24 (94%)	0.31 (6%)	$110 \pm 8$ %
Mg XII(8.42 $\text{\AA}$ )	8.3-8.6	$3.27 \pm 0.14$	1.45	1.00 (91%)	0.10 (9%)	$60 \pm 5$ %
Mg XI(9.17 $\text{\AA}$ )	8.9-9.6	$7.17 \pm 0.19$	2.82	3.00 (76%)	1.19 (24%)	$96 \pm 4$ %
Ne X(12.13 $\text{\AA}$ )	11.9-12.6	$7.61 \pm 0.14$	1.36	4.98 (81%)	1.16 (19%)	$98 \pm 2$ %
Ne IX(13.5 $\text{\AA}$ )	13.2-14.0	$7.51 \pm 0.13$	1.09	3.92 (66%)	2.00 (34%)	$92 \pm 2$ %
Fe XVII(15.1 $\text{\AA}$ )	14.7-15.5	$7.33 \pm 0.13$	0.84	4.78 (82%)	1.05 (18%)	$90 \pm 2$ %
O VIII(16.0 $\text{\AA}$ )	15.7-16.4	$3.26 \pm 0.09$	0.57	2.23 (67%)	1.08 (33%)	$123 \pm 4$ %
Fe XVII(16.9 $\text{\AA}$ )	16.5-17.5	$5.36 \pm 0.11$	0.67	4.19 (97%)	0.12 (3%)	$92 \pm 2$ %
O VIII(19.0 $\text{\AA}$ )	18.5-19.5	$4.54 \pm 0.10$	0.44	1.71 (46%)	2.01 (54%)	$91 \pm 2$ %
O VII(22 $\text{\AA}$ )	20.5-23.0	$3.30 \pm 0.11$	0.53	0.28 (13%)	1.84 (87%)	$77 \pm 3$ %
N VII(24.8 $\text{\AA}$ )	24.6-25.1	$0.64 \pm 0.04$	0.12	0.17 (42%)	0.23 (58%)	$77 \pm 6$ %
C VI(28.5 $\text{\AA}$ )	28.3-28.7	$0.22 \pm 0.05$	0.04	0.02 (13%)	0.13 (87%)	$83 \pm 23$ %

<sup>a</sup> Identified with the dominant components; blending can be significant for some of the features: Ne X(12.13  $\text{\AA}$ ) with Fe XVII, Fe XVII(15.1  $\text{\AA}$ ) with O VIII, O VIII(16.0  $\text{\AA}$ ) with Fe XVIII, and O VIII(19.0  $\text{\AA}$ ) with O VII.

<sup>b</sup> Power law flux plus the continuum flux of the thermal component.

<sup>c</sup> Pure emission line flux of the thermal component and the fraction of its contribution to the emission line.

<sup>d</sup> Percentage of the line flux in the observed spectrum explained by the model: (Thermal+CX)/(Data-Conti)

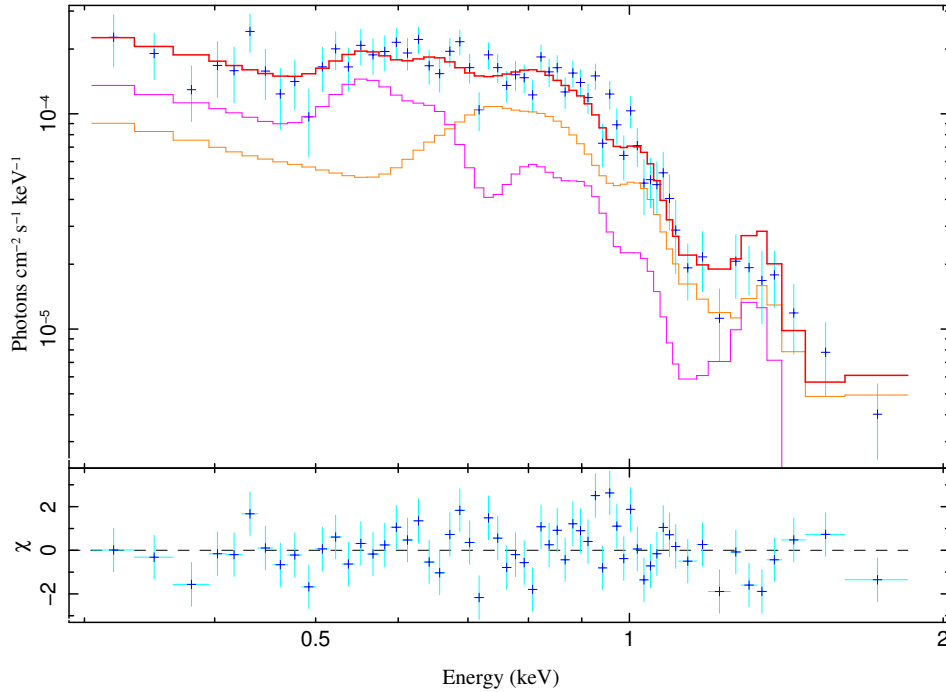


FIG. 4.— EPIC-pn spectrum of the Cap and a fit with a model consisting of the APEC+CX components renormalized from the best fit outflow model. The two components are also shown separately: APEC (orange) and CX (purple).

cause of the poor counting statistics of the C VI (28.5  $\text{\AA}$ ) line. Their lower limit of O is estimated from the plasma-alone modeling of the spectrum (6-18  $\text{\AA}$ ) including the O VIII (16  $\text{\AA}$ ) line. We have shown in the present work (Table 4) that more than half of the line intensities of C, N, O (19  $\text{\AA}$ ) in the RGS spectrum can be attributed to the CX, leading to the reduced abundance estimates of these elements, compared to the results of Ranalli et al. (2008). The absolute Fe abundance that we have measured (Table 4) is lower than theirs again due to the removal of the CX contribution. As a result, our

Ne, Mg and Si to Fe ratios are higher than their results. Similarly, our ratios are all higher than those obtained from the analysis of the *Suzaku* XIS spectra (Konami et al. 2011) based on the thermal model consisting of three temperature components.

For comparison, Figure 5 also includes the abundance patterns expected from core-collapsed SNe in a starburst region. The simulated type Ia SN nucleosynthesis yields (Nomoto et al. 1997) are not shown here, because as expected its X/Fe abundance ratios are much lower compared to our measurements (Fig. 5; Table 2). However,



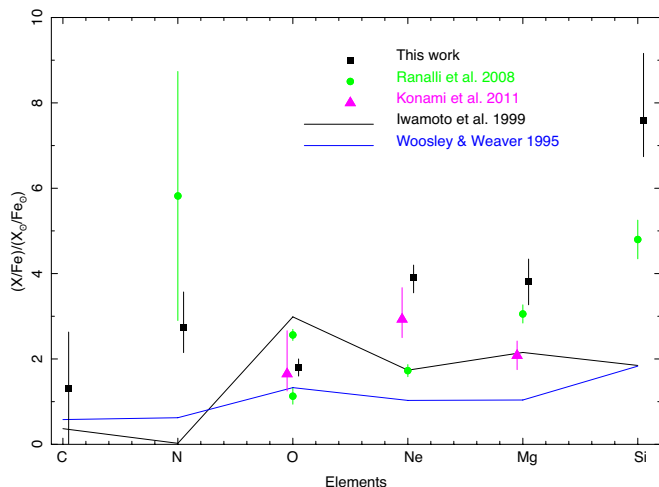


FIG. 5.— X/Fe abundance pattern normalized according to solar values. The black squares mark measurements from this work, the green circles from the RGS study by Ranalli et al. (2008), and the magenta triangles from the *Suzaku* study by Konami et al. (2011). The black line presents the predicted nucleosynthesis yields of type II SNe weighted with the Salpeter IMF in the range of 10–50 solar mass (Iwamoto et al. 1999), while the blue line shows the yields weighted at discrete stellar masses (11, 15, 20, 25, 30, 35 and 40  $M_{\odot}$ ; Woosley & Weaver 1995) but still according to the Salpeter IMF.

our measurements are also systematically higher than the predictions from type II SN yields weighted with the Salpeter initial mass function (IMF) in the range of 10–50 solar mass (Iwamoto et al. 1999) or at discrete stellar masses (11, 15, 20, 25, 30, 35 and 40  $M_{\odot}$ ; Woosley & Weaver 1995). The metal abundances prior to the last burst of star formation can be revealed by those measured for massive stars. The infrared measurements by Origlia et al. (2004) show that  $\text{Fe}/\text{Fe}_{\odot} = 0.46^{+0.26}_{-0.17}$  and  $\text{O}/\text{O}_{\odot} = 1.00^{+0.46}_{-0.32}$ . Any enrichment by stellar winds and SNe would make the abundances higher. However, with the CX considered, we have  $\text{Fe}/\text{Fe}_{\odot} = 0.31 \pm 0.03$  and  $\text{O}/\text{O}_{\odot} = 0.56 \pm 0.05$  (Table 2). Thus, our measurements indicate that the O and Fe depletions may be important even in hot gas. In particular, iron is believed to have the greatest fraction of its atoms depleted into dust grains in cold gas (Savage & Sembach 1996). But dust grains are expected to be destroyed in shocks or sputtered gradually by collisions with electrons in hot gas. A substantial metal depletion in the hot plasma of M82 then suggests that a large fraction of its dust grains didn’t pass a strong shock (e.g., only mass-loaded gently at the interface) and has not been in the hot phase for long (as may be expected for the outflow).

To estimate the density and energetics of the plasma, we need to know its volume. The plasma is considered to be contained approximately in a bi-conic outflow with a half cone opening angle of  $\theta \sim 30^{\circ}$  and a height of  $\sim 3$  kpc (Fig. 1; Melioli et al. 2013), roughly corresponding to the enhanced X-ray region sampled by the RGS data. The total volume of the hot gas is then:

$$\int dV \approx \frac{2\Omega}{4\pi} \frac{4}{3} \pi R^3 = (1 - \cos\theta) \frac{4}{3} \pi R^3 = 5.6 \times 10^{65} \text{ cm}^3,$$

where the  $\Omega$  is the solid angle of each cone opening, and  $R$  is the distance from the galactic center to the top of each cone (assumed to be part of a ball). The top surface

area of the two cones is

$$S_{\text{bottoms}} = \frac{2\Omega}{4\pi} 4\pi R^2 \simeq 10^{44} \text{ cm}^2.$$

With the above volume estimate, we may now infer the mean density of the plasma from the normalization of the APEC model:

$$10^{-14} \int n_e n_H dV / (4\pi D^2) = 0.0062,$$

where  $n_e \simeq 1.2n_H$ , and  $D = 3.52$  Mpc (Table 1) is the distance of M82. Approximating the hot plasma to be homogeneous in the bi-conical outflow, we estimate  $n_H \simeq 0.04 \text{ cm}^{-3}$ . The total mass of the hot plasma is  $M \simeq n_H m_p V = 2 \times 10^7 M_{\odot}$ . Considering the mass deposition rate of  $\sim 14 M_{\odot} \text{ yr}^{-1}$  (§ 5.1), the total mass suggests a period of about 1.4 Myr for the deposition of input materials. Together with the temperature measurement (Table 2), we infer the mean thermal pressure of the plasma as  $P/k \simeq 2n_H T = 5.6 \times 10^5 \text{ K cm}^{-3}$ . This pressure is about 2–20% of the value in the very central region ( $< 300$  pc) of M82,  $P_{\text{center}}/k \sim (0.3 - 3) \times 10^7 \text{ K cm}^{-3}$  (Bregman et al. 1995), and roughly corresponds to the pressure at the radius around 500 pc in the super-wind model (Chevalier & Clegg 1985).

## 5.2. Hot and cool gas interface

With the CX contribution characterized, we can estimate the total incident rate of ions onto the interface and its effective area in the outflow region. From the normalization of the CX model (Table 2), we infer the ion incident rate as  $f_H = \int n_H v dS = 3.2 \times 10^{51} \text{ s}^{-1}$ , or about 80  $M_{\odot}$  hot ions per year. Together with our model temperature, it implies that the CX involves a thermal energy of about  $3k_B T f_H \simeq 10^{43} \text{ ergs s}^{-1}$  (including the contribution from electrons), which is comparable to the total expected mechanical energy input from SWs and SNe of about  $10^{43} \text{ ergs s}^{-1}$  (Strickland & Heckman 2009). This indicates that the CX is a manifestation of the substantial heat exchange between the hot and cool gases.

According to the conventional superwind modeling of the outflow from M82, the hot gas in the outflow region would have a velocity  $\gtrsim 10^3 \text{ km s}^{-1}$ , while the entrained cool gas moves slowly (e.g.,  $\sim 500 \text{ km s}^{-1}$ ; Melioli et al. 2013). In reality, the free expanding superwind modeling may work only partly in M82, perhaps in the northern side of the galaxy (Liu et al. 2012), which is evidenced by the presence of the Cap (Lehnert et al. 1999). A good fraction of the hot plasma, especially in the southern side of the galaxy, seems to be morphologically enclosed by cool gas, as seen in images of  $\text{H}\alpha$ , dust radiation, and X-ray. Nevertheless, a good approximation of the relative velocity may be  $v \sim 500 \text{ km s}^{-1}$ , comparable to the sound velocity of the hot plasma. Then with  $n_H \sim 0.04 \text{ cm}^{-3}$ , as obtained above for the hot plasma, we estimate the total effective area of the interface as  $\int dS \sim 2 \times 10^{45} \text{ cm}^2$ . This area is about one order of magnitude larger than the summed cross-section of the two cones, consistent with the turbulent nature of the interface around cool gas clouds/filaments embedded in the hot plasma, and along the outer boundaries of the cones. The enlarged interface confines the outflow from free-expanding, and makes the mass-loading into the hot gas efficient (Rogers & Pittard 2013).

How various potential astrophysical processes actually occur at the cool/hot interface remains somewhat uncertain. A layer of turbulent mixing may exist over the interface region driven by various instabilities, with a characteristic length scale of a few parsecs (Slavin et al. 1993). Also turbulence by its nature generates eddies cascading from macroscopic scales down to smaller ones. The processes such as CX and thermal conduction can operate efficiently on those microscopic scales. For a typical CX length scale of  $\sim 10^{15}$  cm, the saturated thermal conduction by electrons may occur on time scales of about one year (Cowie & McKee 1977). Given the relative velocity as  $500 \text{ km s}^{-1}$ , the CX occurs on a similar time scale. Unlike thermal conduction, neutral atoms can move across magnetic fields or can thus be shaken out cool gas clouds in a highly turbulent environment, resulting microscopic mixing of gases in different phases. In particular, since the ionization time scale of hydrogen is about ten years, the CX can proceed efficiently.

### 5.3. Cap as a discrete interface

The Cap potentially provides the cleanest site to test the CX scenario and to probe the properties of the outflow from M82. At a distance sufficiently far from the starburst nucleus of the galaxy, this distinct feature should have a relatively uniform foreground absorption, which remains a systematic uncertainty in the analysis of the outflow region, and is largely free from contamination of discrete sources. Most importantly, the morphology of the reflected UV radiation, as well as those of the X-ray and  $\text{H}\alpha$  emissions, all indicate that a discrete interface exists between the relatively isolated cool gas filament and the hot outflow, which is otherwise difficult to detect at the large distance from the galactic disk. The impact of the outflow on the filament should naturally lead to the CX, as suggested by Lallement (2004). Although the existing X-ray observations provide no distinct spectral line signature to quantify the CX contribution, the overall spectral consistency of the filament with the outflow is encouraging. The results from the Cap and outflow regions together can further be used to place additional constraints on the properties of the outflow at the distance of the Cap.

Similar to what we have done above for the outflow region near the disk (§ 5.2), we can infer the ion incident rate into the Cap as  $6.2 \times 10^{49} \text{ s}^{-1}$  from the measured spectral normalization (Table 2). If we assume the outflow density of  $\sim 0.04 \text{ cm}^{-3}$  and the absolute velocity of  $\sim 1000 \text{ km s}^{-1}$  at 3 kpc, plus the solid angle of the cone  $\Omega = 0.84 \text{ sr}$ , we may estimate the upper limit of the outflow ion particle flux as  $\sim 2.4 \times 10^{50} \text{ s}^{-1} \text{ sr}^{-1}$ . Together with the above ion incident rate and the off-galaxy center distance of the Cap as 11.6 kpc, we infer the lower limit of its interacting surface area as  $\sim 3 \times 10^7 \text{ pc}^2$ . However, assuming the outflow-facing Cap to be approximately a circle of  $1.8'$  radius (Lehnert et al. 1999), the surface area would be roughly  $10^7 \text{ pc}^2$ . The discrepancy between the two areas indicates that either the Cap is elongated along our line of sight.

### 5.4. Correlation between soft X-ray and $\text{H}\alpha$ emissions

The presence of the CX naturally leads to the prediction of its contribution to the  $\text{H}\alpha$  emission, in addition to

the soft X-ray line emission that we have focused on. A hot proton undergoing a CX has a  $\sim 20\%$  probability to produce an  $\text{H}\alpha$  photon (Raymond 2012; Lallement 2012). For the outflow region, the above estimated hot proton incident rate,  $3.2 \times 10^{51} \text{ s}^{-1}$ , can be translated into an  $\text{H}\alpha$  flux of  $0.43 \text{ photon s}^{-1} \text{ cm}^{-2}$ , or  $1.3 \times 10^{-12} \text{ erg s}^{-1} \text{ cm}^{-2}$ . This CX contribution is about 3% of the observed  $\text{H}\alpha$  flux from the entire M82 (Lehnert et al. 1999) and may be responsible for much of the broadest  $\text{H}\alpha$  line component with the measured  $\text{FWHM} = 333 \text{ km s}^{-1}$  (Table 2 in Westmoquette et al. 2009). This width is smaller than the thermal broadening of the 0.6 keV plasma with a  $\text{FWHM}$  of  $\sqrt{8kT\ln 2/m_p} = 560 \text{ km s}^{-1}$ , where  $m_p$  is the mass of proton. But the velocity decomposition of the  $\text{H}\alpha$  line can be quite uncertain (e.g., sensitive to the specific way in which the observed line is decomposed). We may also expect that the shock driven into the cool gas from the impact of the high-speed outflow be responsible for part of the  $\text{H}\alpha$  emission, as well as the perhaps dominant contribution from the recombination of photoionized gas. But still, the broadest  $\text{H}\alpha$  component in the outflow region could be largely a result of the CX. In the Cap region, the CX contribution increases to 17% of the observed  $\text{H}\alpha$  flux.

A spatial correlation between the diffuse X-ray and  $\text{H}\alpha$  emissions was noted previously in M82 and other nearby star-forming galaxies (e.g., Strickland et al. 2000b, 2004). This correlation led to the impression that both the soft X-ray emission and the  $\text{H}\alpha$  emission may largely arise at boundaries between the hot and cold gases, occupying a small percentage of the space. But the specific mechanism for such interaction is not clear, although shock (Strickland & Stevens 2000a) and thermal conductions (e.g. D’Ercole & Brighenti 1999) have been proposed. Even with an outflow velocity of  $\sim 10^3 \text{ km s}^{-1}$ , it is not clear that the forward-shock propagating into the entrained dense cool gas would be energetic enough to produce X-ray-emitting plasma. Furthermore, it has been shown that the correlation is valid only globally; locally the X-ray enhancements can be anti-correlated with  $\text{H}\alpha$  features (Liu et al. 2012). This anti-correlation cannot easily be brought into a consistency with the shock heating interpretation.

In our model, about a quarter of the total observed X-ray emission in the 0.4-2 keV band arises from the CX emission at the interface. This specific mechanism provides a natural explanation for the global correlation between the soft X-ray and  $\text{H}\alpha$  emissions, while the local anti-correlation is expected for the X-ray emission from volume-filling thermal plasma enclosed by  $\text{H}\alpha$ -emitting cool gas.

## 6. SUMMARY AND CONCLUSION

We have made the first attempt to characterize the soft X-ray emission from M82 with a simple physical spectral model. A novel component of this model is the implementation of the CX contribution, joined with a volume-filling, one-temperature, thermal plasma (APEC). This APEC+CX model is used to fit both the entire RGS spectrum of the central outflow and the EPIC-pn spectrum of the Cap region. We summarize the main results and conclusions as follows:

- The model fits the RGS spectrum of the outflow

well to an accuracy of matching individual emission features typically within 25%. The fit shows that the CX is largely responsible for the enhanced forbidden lines of the  $K\alpha$  triplets of various He-like ions, and contributes substantially to the  $Ly\alpha$  transitions of C VI ( $\sim 87\%$ ), O VIII and N VII ( $\gtrsim 50\%$ ). About a quarter of the X-ray flux in the 6-30 Å band originates in the CX. Furthermore, the required CX rate gives a direct estimate of the equivalent hot proton flux of  $3.2 \times 10^{51} \text{ s}^{-1}$ , which undergoes the CX at the hot and cool gas interface.

- The separation of the CX contribution improves the measurements of the thermal and chemical properties of the volume-filling plasma. The measured temperature of 0.6 keV is at the high end of the range inferred from the previous modeling with thermal plasma only, albeit with multiple temperature components. The mean density of the plasma is  $\sim 0.04 \text{ cm}^{-3}$  and its total mass is  $\sim 2 \times 10^7 M_{\odot}$  within the inner  $\sim 3$  kpc region. Our measured metal abundances are close to be solar (typically within a factor of  $\sim 2$ ) and show significant deviations from those based on thermal plasma-only modeling. The abundance pattern of X/Fe is systematically higher than the nucleosynthetic yields of core-collapsed SNe, suggesting Fe depletion onto dust grains even in the hot plasma.
- A substantial mass-loading, a factor of  $\sim 10$  of the SN and SW injected mass injection, from cool gas to hot plasma is inferred over the entire outflow region sampled by the RGS. This mass-loading is required to explain the low temperature and high density of the plasma. The CX may just be a by-product of the mass-loading and may be responsible for much of the required heating of the cool gas, as indicated by a substantial energy flux involved in the process (comparable to the total mechanical energy input from the stars).
- Assuming a characteristic relative velocity  $\sim 500 \text{ km s}^{-1}$  (comparable to the sound velocity of the hot gas) between the hot and cool gases, we estimate the effective area of the interface as  $\sim 2 \times 10^{45} \text{ cm}^2$ , or one order of magnitude larger than the geometrical cross-section of the bi-conic outflows at 3 kpc off the galactic nucleus. This large area of the interface is expected from the embedding of many cool gas clouds/filaments in the hot plasma and from the turbulent mixing between the two gas phases and can naturally accommodate substantial mass-loading to the hot plasma.
- The EPIC spectrum of the Cap, as the most natural location for the CX process, can be well characterized by the same APEC+CX model (that best-fits the RGS spectrum of the outflow region) with a simple fitting to the normalizations. The CX contributes nearly half of the X-ray flux of the Cap in

the 6 - 30 Å band, which requires an ion incident rate of  $6.2 \times 10^{49} \text{ s}^{-1}$ . The Cap may be elongated along our line of sight to account for this ion incident rate.

- Our model naturally explains the global spatial correlation and some local anti-correlation between the X-ray and  $H\alpha$  emissions. The local anti-correlation, apparent only in some regions, likely reflects the fact that the volume-filling hot plasma is surrounded and possibly enclosed by cool ( $H\alpha$ -emitting) gas across the bulk of the field. But the anti-correlation is weakened by the CX contribution to the X-ray emission, especially in the very soft X-ray band. On scales greater than individual bubbles/shells or other intermixing structures, the global correlation is expected. While the overall intensity of the  $H\alpha$  emission is dominated by photoionization, plus shocking heating, the CX of hot protons with neutral atoms could still be considerable (likely a few to twenty percent of the emission) and may be largely responsible for the broadest component of the observed  $H\alpha$  emission line.

While the main goal of the present work is to demonstrate the potential utility of the CX spectral model in characterizing the soft X-ray line emission from a starburst galaxy, clearly more work needs to be done. In particular, we have only modeled the integrated RGS spectrum of the outflow. The unfavorable dispersion direction of the existing RGS observations does not allow us to probe the outflow structure along the galaxy's minor axis. Thus a deep *XMM-Newton*/RGS observation with the dispersion perpendicular to the minor axis is highly desirable. With imaging spectroscopic capability of upcoming X-ray detectors (e.g., *Astro-H*), major advances can be made with the type of modeling illustrated here, which will lead to improved measurements of the plasma properties and unique insights into the interplay between hot and cool gases in such galaxies. Finally, we also plan to carefully examine scenarios other than the CX and the thermal plasma emissions (e.g., recombining plasma due to fast adiabatic expansion or to a recently extinguished active galactic nucleus), although they were not favored in brief explorations (e.g. Liu et al. 2012).

#### ACKNOWLEDGEMENTS

We gratefully acknowledge the anonymous referee for their comments that improved this paper. We thank John Houck for help on solving all ISIS software problems, and thank Keith Arnaud for help on the installation of the RGSXSRC script that is removed from the 12.7 version of Xspec. The work is partly supported by the National Natural Science Foundation of China under the grant 11203080, and by the Smithsonian Institution's Competitive Grants for Science. Li Ji is also supported by the 100 Talents program of Chinese Academy of Sciences.

#### REFERENCES

- Anders, E., & Grevesse, N. 1989, *Geochim. Cosmochim. Acta*, 53, 197
- Beiersdorfer, P., Boyce, K. R., Brown, G. V., et al. 2003, *Science*, 300, 1558

- Bregman, J. N., Schulman, E., & Tomisaka, K. 1995, *ApJ*, 439, 155
- Chevalier, R. A., & Clegg, A. W. 1985, *Nature*, 317, 44
- Cowie, L. L., & McKee, C. F. 1977, *ApJ*, 211, 135
- D’Ercole, A., & Brighenti, F. 1999, *MNRAS*, 309, 941
- Devine, D., & Bally, J. 1999, *ApJ*, 510, 197
- Dickey, J. M., & Lockman, F. J. 1990, *ARA&A*, 28, 215
- Engelbracht, C. W., Kundurthy, P., Gordon, K. D., et al. 2006, *ApJ*, 642, L127
- Fabbiano, G. 1988, *ApJ*, 330, 672
- Foster, A. R., Ji, L., Smith, R. K., & Brickhouse, N. S. 2012, *ApJ*, 756, 128
- Guenou, C., Auchère, F., Klimchuk, J. A., Bocchialini, K., & Parenti, S. 2013, *ApJ*, 774, 31
- Griffiths, R. E., Ptak, A., Feigelson, E. D., et al. 2000, *Science*, 290, 1325
- Heckman, T. M., Armus, L., & Miley, G. K. 1990, *ApJS*, 74, 833
- Heckman, T. M. 2005, *Starbursts: From 30 Doradus to Lyman Break Galaxies*, 329, 3
- den Herder, J. W., Brinkman, A. C., Kahn, S. M., et al. 2001, *A&A*, 365, L7
- Hoopes, C. G., Heckman, T. M., Strickland, D. K., et al. 2005, *ApJ*, 619, L99
- Houck, J. C. 2002, *High Resolution X-ray Spectroscopy with XMM-Newton and Chandra*, MSSL, 24-25 October 2002
- Iwamoto, K., Brachwitz, F., Nomoto, K., et al. 1999, *ApJS*, 125, 439
- Jacobs, B. A., Rizzi, L., Tully, R. B., et al. 2009, *AJ*, 138, 332
- Janev, R. K., & Winter, H. 1985, *Physics Reports*, 117, 265
- Konami, S., Matsushita, K., Tsuru, T. G., Gandhi, P., & Tamagawa, T. 2011, *PASJ*, 63, 913
- Lallement, R. 2004, *A&A*, 422, 391
- Lallement, R. 2012, *Astronomische Nachrichten*, 333, 347
- Lehnert, M. D., Heckman, T. M., & Weaver, K. A. 1999, *ApJ*, 523, 575
- Liu, J., Wang, Q. D., & Mao, S. 2012, *Astronomische Nachrichten*, 333, 365
- Lynds, C. R., & Sandage, A. R. 1963, *ApJ*, 137, 1005
- Mathews, W. G., & Baker, J. C. 1971, *ApJ*, 170, 241
- Matsumoto, H., Tsuru, T. G., Koyama, K., et al. 2001, *ApJ*, 547, L25
- Melioli, C., de Gouveia Dal Pino, E. M., & Geraissate, F. 2013, *arXiv:1301.5005*
- Nomoto, K., Iwamoto, K., Nakasato, N., et al. 1997, *Nuclear Physics A*, 621, 467
- Origlia, L., Ranalli, P., Comastri, A., & Maiolino, R. 2004, *ApJ*, 606, 862
- Ranalli, P., Comastri, A., Origlia, L., & Maiolino, R. 2008, *MNRAS*, 386, 1464
- Raymond, J. C. 2012, *Astronomische Nachrichten*, 333, 290
- Read, A. M., & Stevens, I. R. 2002, *MNRAS*, 335, L36
- Rogers, H., & Pittard, J. M. 2013, *MNRAS*, 431, 1337
- Savage, B. D., & Sembach, K. R. 1996, *ARA&A*, 34, 279
- Shoppell, P. L., & Bland-Hawthorn, J. 1998, *ApJ*, 493, 129
- Slavin, J. D., Shull, J. M., & Begelman, M. C. 1993, *ApJ*, 407, 83
- Smith, R. K., Foster, A. R., & Brickhouse, N. S. 2012, *Astronomische Nachrichten*, 333, 301
- Smith, R. K., Foster, A. R., Edgar, R. J. & Brickhouse, N. S. 2014, *ApJ*, in press.
- Strickland, D. K., & Stevens, I. R. 2000a, *MNRAS*, 314, 511
- Strickland, D. K., Heckman, T. M., Weaver, K. A., & Dahlem, M. 2000b, *AJ*, 120, 2965
- Strickland, D. K., Heckman, T. M., Weaver, K. A., Hoopes, C. G., & Dahlem, M. 2002, *ApJ*, 568, 689
- Strickland, D. K., Heckman, T. M., Colbert, E. J. M., Hoopes, C. G., & Weaver, K. A. 2004, *ApJS*, 151, 193
- Strickland, D. K., & Heckman, T. M. 2009, *ApJ*, 697, 2030
- Suchkov, A. A., Berman, V. G., Heckman, T. M., & Balsara, D. S. 1996, *ApJ*, 463, 528
- Taylor, C. L., Walter, F., & Yun, M. S. 2001, *ApJ*, 562, L43
- Tsuru, T. G., Ozawa, M., Hyodo, Y., et al. 2007, *PASJ*, 59, 269
- Veilleux, S., Cecil, G., & Bland-Hawthorn, J. 2005, *ARA&A*, 43, 769
- Westmoquette, M. S., Gallagher, J. S., Smith, L. J., et al. 2009, *ApJ*, 706, 1571
- Wilms, J., Allen, A., & McCray, R. 2000, *ApJ*, 542, 914
- Woosley, S. E., & Weaver, T. A. 1995, *ApJS*, 101, 181